Nanocomposite Architecture for Rapid, Spectrally-Selective Electrochromic Modulation of Solar Transmittance

Jongwook Kim,[†] Gary K. Ong,[†,‡] Yang Wang,[†] Gabriel LeBlanc,[†] Teresa E. Williams,[§,‖] Tracy M. Mattox,[‖] Brett A. Helms,[‖] and Delia J. Milliron*,[†]

[†]McKetta Department of Chemical Engineering, University of Texas at Austin, Austin, Texas 78712, United States
[‡]Department of Materials Science & Engineering, University of California, Berkeley, Berkeley, California 94720, United States
[§]Graduate Group in Applied Science & Technology, University of California, Berkeley, Berkeley, California 94720, United States
[‖]The Molecular Foundry, Lawrence Berkeley National Laboratory, Berkeley, California 94720, United States

S *Supporting Information*

ABSTRACT: Two active electrochromic materials, vacancy-doped tungsten oxide (WO_{3-x}) nanocrystals and amorphous niobium oxide (NbO_x) glass are arranged into a mesostructured architecture. In a strategy applicable across electrochemical applications, the critical dimensions and interfacial connections in the nanocomposite are designed to optimize pathways for electrochemical charging and discharging. The result is an unprecedented optical range for modulation of visible and near-infrared solar radiation with rapid switching kinetics that indicate the WO_{3-x} nanocrystal framework effectively pumps charge out of the normally sluggish NbO_x glass. The material is durable for at least 2000 electrochemical cycles.
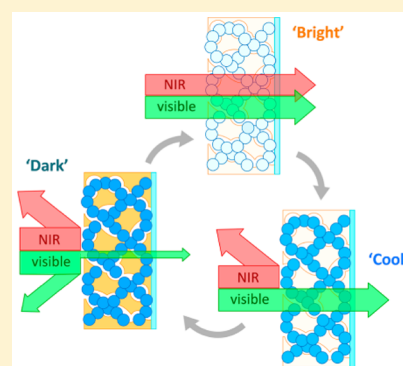
KEYWORDS: *electrochromic, nanocomposite architecture, plasmonic nanocrystals, block copolymer templated assembly*

In principle, composite materials can combine and enhance the advantageous properties of two or more components. In practice, judicious arrangement of matter is essential to avoid deleterious interactions that can result from simple blending.[1] In nanoscale composites, structural organization takes on even greater importance as distinct physical and chemical properties can emerge from confinement and from the high density of interfaces. Significant performance gains therefore can be realized when the critical length scales and spatial relationships in nanocomposite materials are deliberately designed and fabricated, or architected, to meet a functional purpose.

Electrochemical and photochemical systems (e.g., batteries, fuel cells, photovoltaic cells, and electrochromic devices) have long been major targets for exerting control over nanoscale architecture in the effort to meet complex performance criteria, which requires coordinated and efficient transport of electrons, ions, and molecular species.[2−8] In some of the most elegant examples of architected composites, battery electrodes with both high rate capability and high capacity have been constructed by using an electronically conductive mesostructured framework to mechanically support and "wire up" an insulating, but high-capacity active material.[1,4] In these examples, the framework component is selected to mitigate a deficiency (poor electronic conductivity) of the active material. In other instances, two active materials with complementary properties have been blended to form a large interfacial area central to the material's functionality. This is the case for polymer blend photovoltaic cells, where n- and p-type semiconducting polymers transfer charge across the interface,[9,10] and for our recently reported nanocrystal-in-glass electrochromic materials, in which the interface between near-infrared- and visible-light modulating components enhances the optical switching contrast.[11] However, the random mixing of components in active material blends can be detrimental, because transport pathways are tortuous and can contain dead ends. Such composites could benefit from more deliberate architecting of their mesoscale structure.[12] In the example elaborated here, we describe a nanocomposite metal oxide electrochromic material that utilizes a templated mesoscale architecture to achieve rapid switching and unprecedented dynamic range for modulating visible (VIS) and near-infrared (NIR) transmittance.

We recently established that degenerately doped metal oxide nanocrystals can effectively modulate NIR transmittance through electrochemical charging and discharging of the free electrons responsible for their localized surface plasmon resonance (LSPR) absorption.[13,14] Considering the fact that solar NIR is most intense at shorter wavelengths (700−1300 nm, Supporting Information Figure S1), we hypothesized that
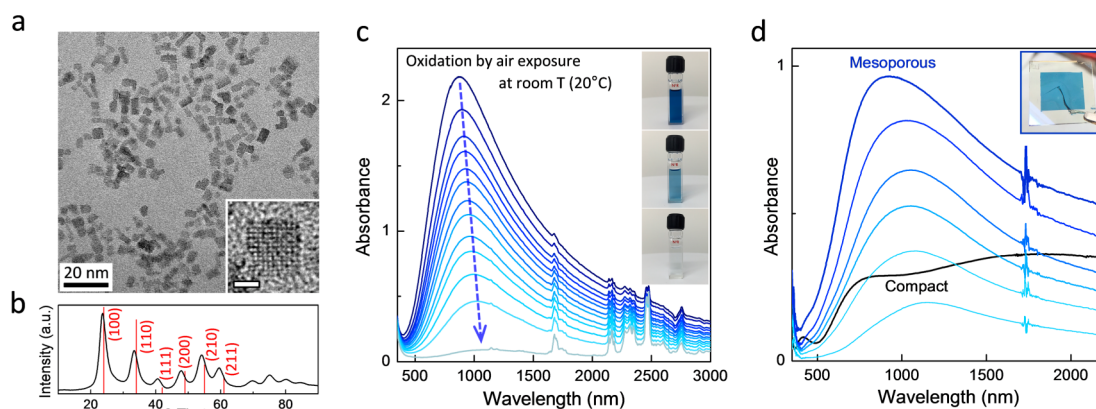
5574

Figure 1. Tungsten oxide nanocrystals for NIR modulation. (a) Low- and high-resolution transmission electron microscopy (TEM). The scale bar in the inset image is 2 nm. (b) X-ray diffraction pattern of the synthesized WO_{3-x} nanocrystals (black) and the reference pattern for the cubic WO_3 phase (indexed red bars, JCPDS 041−0905). (c) VIS-NIR absorbance spectra of a colloidal solution in tetrachloroethylene. The spectra were acquired 0, 1, 5, 10, 20, 30, 50, 70, 110, 150, 235, 380, and 1300 min after exposure to air (from top to bottom). The inset pictures show the solution cuvette used for this measurement at 0, 50, and 1300 min. (d) Electrochemically switched [vs Li/Li+ in 0.1 M Li-TFSI/tetraglyme] absorbance spectra of WO_{3-x} nanocrystal films on ITO coated glass. Blue lines are for a mesoporous film prepared by block copolymer templated assembly (thickness = 280 nm, porosity = 71%), showing a gradual increase of the LSPR peak with a blue-shift ($\Delta\lambda \sim 250$ nm) at different charging states. Black line is for a randomly packed film (saturated at 1.5 V) prepared with the same volume of WO_{3-x} nanocrystals per unit area (thickness = 108 nm, porosity = 28%). The inset picture shows a fully charged mesoporous film sample.
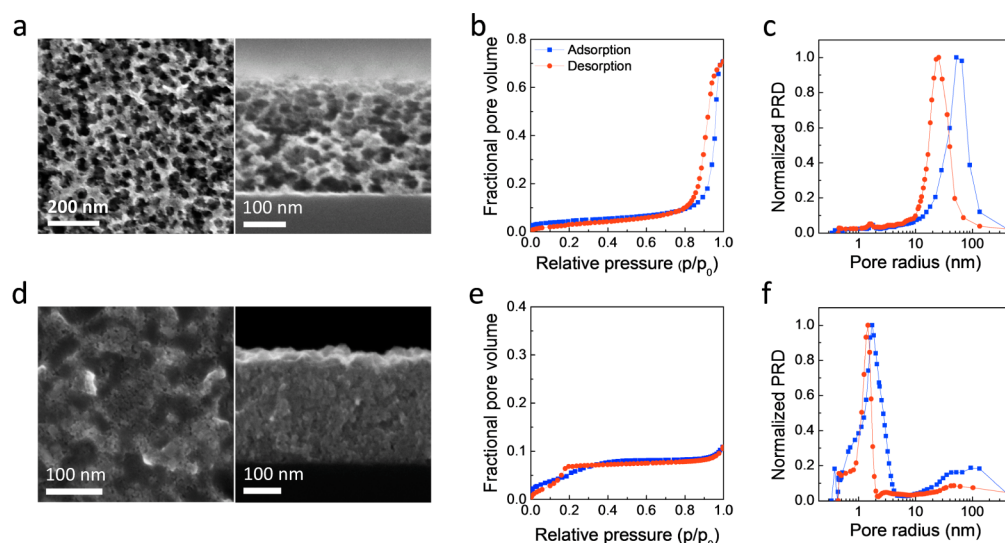

Figure 2. Mesoporous (WO_{3-x}) and nanocomposite (WO_{3-x}−NbO_x) architectures. Scanning electron microscopy (SEM) images (left: top down, right: cross section) of (a) a mesoporous WO_{3-x} nanocrystal framework film, and (d) an architected composite film after in-filling with NbO_x glass. Toluene adsorption−desorption isotherms for (b) the mesoporous WO_{3-x} framework and (e) the composite, and (c), (f) the respective normalized pore radius distributions (PRD).

nanocrystals with LSPR absorption in this spectral range would be ideal for dynamic solar control. To this end, we selected WO_{3-x} nanocrystals to serve as the first active component in our nanocomposite architecture. Both interstitially doped and oxygen vacancy-doped tungsten oxide nanocrystals[15,16] can exhibit LSPRs at shorter wavelength than substitutionally doped transparent conducting oxides such as tin-doped indium oxide (ITO)[17−19] or aluminum-doped zinc oxide (AZO).[20] We developed a synthetic route for WO_{3-x} nanocrystals (Figure 1a) with a small average size (4.3 ± 1.3 nm, Supporting Information Figure S2). Based on our prior work with ITO nanocrystals we expect these small nanocrystals to produce the strongest optical modulation when electrochemically charged.[13] Examining the X-ray diffraction pattern of the WO_{3-x} nanocrystals (Figure 1b), their lattice is significantly distorted

from the cubic WO_3 phase. We ascribe that distortion to a large number of oxygen vacancies, which generate a strong LSPR absorption peak centered at 875 nm in wavelength (Figure 1c). This LSPR band overlaps well with the NIR region of the solar spectrum (Supporting Information Figure S1) while maintaining relatively high VIS (390−700 nm) transparency with minor absorption in the red range. The series of LSPR spectra in Figure 1c show fast oxidative decay under air exposure followed by a red-shift ($\Delta\lambda \sim 200$ nm) and finally bleaching to a fully transparent state. This rapid environmental response is likely facilitated by the small nanocrystal size, which we hypothesized should likewise enable fast electrochemical modulation of the LSPR.[13,14]

In fact, we found that it was necessary to arrange the WO_{3-x} nanocrystals into a mesoporous architecture in order to realize

an electrochromic response that resembled the spectral response found in solution (Figure 1d). To do so, WO_{3-x} nanocrystals were assembled by means of a sacrificial micellar block copolymer (poly(N,N-dimethylacrylamide)-b-polystyrene, PDMA-b-PS) architecture-directing agent. PDMA-b-PS micelles are unique in their ability to provide access to well-ordered colloidal nanocrystal frameworks from ligand-stripped nanocrystals by assembling these components in solution, then creating a nanocrystal-polymer composite architecture film by spin-coating.[21] After thermal removal of the block copolymer micelles, the assembled framework contains densely distributed spherical mesopores visible by SEM (Figure 2a). Analysis by ellipsometric porosimetry[22] (Figure 2b,c, Table 1, and

Table 1. Characteristics of Pore Networks in Electrochromic Films Characterized by Ellipsometric Porosimetry

	porosity (%)	pore radius, cage (nm)	pore radius, neck (nm)
random packed WO_{3-x}	28	5.7	3.7
mesoporous WO_{3-x}	71	53	26
mesostructured WO_{3-x}–NbO_x	9	1.7	1.5
pure NbO_x	0	n/a	n/a

Supporting Information Figure S5) reveals the mesoscale pore size (53 nm-cage and 26 nm-neck) and the high porosity (71%) of the WO_{3-x} nanocrystal framework, which can be compared to a randomly packed film of the same nanocrystals that has smaller pores (5.7 nm-cage and 3.7 nm-neck) and lower porosity (28%).

When electrochemically charged with Li^+ ions, WO_{3-x} nanocrystals deposited on the working electrode (ITO coated glass) acquire electrons as free carriers generating the LSPR. The mesoporous WO_{3-x} framework film exhibits rapid and reversible plasmonic electrochromism upon cycling (Figure 1d) showing spectral changes similar to those of the environmental oxidation process shown in Figure 1c. By contrast, a nanocrystal film made without the block copolymer shows a broad, red-shifted optical response that can be explained by strong LSPR coupling among the nanocrystals, which are densely packed in three dimensions.[23] The mesostructured film has a clear aspect without haziness in both colored and bleached states, consistent with the mesopore dimensions lying far below the visible wavelengths. The specific charge capacity of the nanocrystal framework is more than double that of a dense nanocrystal film (16.2 vs 7.5 mC/cm^2) with the same loading, facilitating strong modulation of the LSPR.[24] To better understand the origin of electrochromism in the frameworks, a purely capacitive charging process was enforced by using an electrolyte containing bulky molecular cations (tetrabutylammonium, TBA^+), which cannot intercalate into the crystal lattice. The coloration using TBA-TFSI was 84% of that using Li-TFSI, indicating that capacitive charging can account for most of the light absorbance (Supporting Information Figure S3). A high level of the capacitive contribution has similarly been reported for few-nanometer diameter TiO_2 nanocrystals.[25] The strong, NIR-selective modulation obtained with plasmonic WO_{3-x} nanocrystal frameworks therefore is distinguished from the electrochromism typically found in amorphous and mixed-phase tungsten oxide films, which have a broader characteristic spectrum that may include contributions due to polaronic absorption.[26,27]

To complement the NIR optical response of the WO_{3-x} nanocrystals, a second active component, amorphous NbO_x, was selected that exhibits electrochromism mostly in the VIS range. NbO_x glass was similarly used in our previous work as the visible light-modulating component of ITO nanocrystal-in-glass electrochromic composite films.[11] When NbO_x is electrochemically charged, localized polaronic states give rise to its characteristic absorption,[11,28] which increases in extinction at shorter visible wavelengths so that the film has a brown tint (Supporting Information Figure S3). This spectrum makes an ideal complement to the red-to-NIR plasmonic absorption of electrochemically charged WO_{3-x} (Figure 1d); together, the absorption of these two component materials can cover the full spectrum of solar radiation. Thermal decomposition of the poyloxometalate (POM) cluster salt, $(NMe_4)_6[Nb_{10}O_{28}]\cdot6H_2O$,[29] is a convenient route to electrochromic NbO_x glass, particularly as this POM is water-soluble. Optical quality films were prepared by spin-coating from aqueous ethanol (1:1 mixture) then annealing at 400 °C.[11]

To organize these two ideal electrochromic components—WO_{3-x} nanocrystals for NIR control and NbO_x for visible light control—into an architected nanocomposite, the mesopores of a WO_{3-x} nanocrystal framework were backfilled with POM. After annealing, an interpenetrating glass network was formed within the WO_{3-x} nanocrystal framework.[30] The mostly dense composite is found by ellipsometric porosimetry (Figure 2e,f and Table 1) to be 9% porous. The small mesopores detected by porosimetry (1.7 nm cages and 1.5 nm necks) are seen by SEM to be open at the film surface (Figure 2d).

Upon electrochemical charging, the NbO_x-filled WO_{3-x} composite architecture exhibits completely independent and reversible electrochromic switching of the two metal oxide components. The transmittance spectra of the 260 nm-thick composite film reveal dual-band VIS and NIR modulation at different charging voltages (Figure 3a). When applying 4 V [vs. Li/Li^+], the film is transparent both in the NIR and VIS ranges ("bright mode") as both WO_{3-x} and NbO_x are fully discharged. At 2.3 V, WO_{3-x} nanocrystals are selectively charged, recovering free electrons that give rise to LSPR absorption in the NIR range. In this "cool mode", the film blocks most of the transmission in the NIR range; in a typical commercial or residential window, this would reduce solar heat gain while maintaining a high VIS transmittance useful for daylighting[31] (Table 2). At 1.5 V, NbO_x is reduced by Li^+ ion intercalation inducing polaronic absorption of VIS light, resulting in a "dark mode". The short wavelength absorption tail of the further charged WO_{3-x} also contributes to VIS (red edge) blocking in the dark mode, optimally complementing the NbO_x spectrum to produce a largely neutral tint (Figures 3a).[32] The color indices (CIELab space) calculated from the dark-mode spectrum ($L^* = 54$, $a^* = -11$, $b^* = -22$) indicate a blue-gray color that is aesthetically desirable for window applications. Earlier studies on electrochromic materials have focused on single-band VIS modulation mostly achieving a limited dark mode transmittance value or poor color neutrality.[33] NIR transmission has so far been controlled most successfully with static coatings. Our composite film is the first dual-band electrochromic material with an unprecedented dynamic optical range and VIS-NIR selectivity satisfying the optical performance criteria for practical energy-saving smart windows.

Despite its low 9% porosity, the architected composite is very active electrochemically and exhibits higher optical contrast
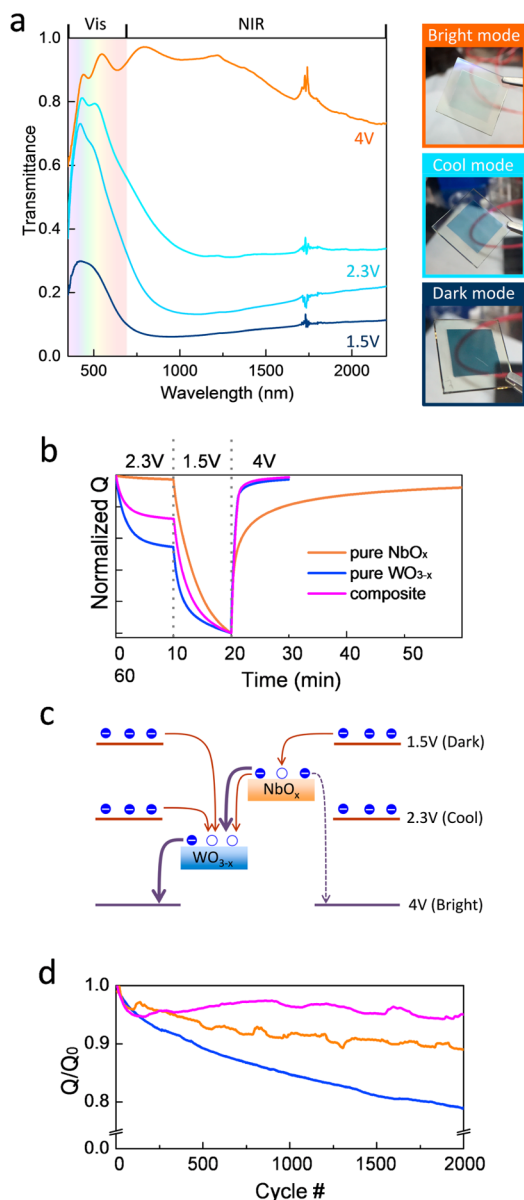
Table 2. Integrated Solar Transmittances in the VIS, NIR, and Total Solar[a] Ranges for the Architected Composite Film Shown in Figure 3a

mode	T_{VIS}	T_{NIR}	T_{sol}
bright	0.93	0.91	0.92
cool (1 min)	0.73	0.36	0.54
cool (3 min)	0.54	0.16	0.35
dark	0.22	0.07	0.14

[a]Abbreviateed "sol".

randomly packed WO_{3-x} nanocrystal film and 80% of the that found in the 70% porous WO_{3-x} framework (based on the integrated absorbance between 450−2200 nm wavelength). Meanwhile, in the architected composite NbO_x obtains a 1.4-fold enhancement of optical contrast (absorbance at λ = 450 nm) compared to a pure NbO_x film, which may reflect structural changes to the glass network, as observed in our previous work on randomly structured nanocrystal-in-glass composites.[11]

Besides this high optical contrast, the architected composite exhibits remarkably rapid switching; most notably the discharging of NbO_x is dramatically accelerated compared to pure NbO_x. It has been reported that switching time for tungsten oxide films can be reduced down to several seconds by introducing mesoporous structures.[34,35] Switching of a WO_{3-x} nanocrystal film is thus typically much faster than that of a compact NbO_x film (Figure 3b). Within the architecture, however, the spectral signature of reduced NbO_x is the first to bleach, indicating NbO_x is discharged first, followed by the WO_{3-x} component (Supporting Information Figure S6). In fact, both components can be discharged as rapidly as a pure WO_{3-x} mesoporous framework (Figure 3b). The fast kinetics and high optical contrast suggest efficient access by the electrolyte to the active materials in the composite architecture. We hypothesize that small mesoporous channels are effectively templated along the WO_{3-x} framework during POM decomposition. The similar neck and cage dimensions observed by ellipsometric porosimetry are consistent with the presence of a highly efficient network of porous channels that permit electrolyte access so that Li^+ ions can be transferred across all three interfaces ($WO_{3-x} \leftrightarrow NbO_x$, $WO_{3-x} \leftrightarrow$ electrolyte, $NbO_x \leftrightarrow$ electrolyte), allowing the most kinetically facile pathway to be autonomously selected. Therefore, as depicted in Figure 3c, a cascade discharging of NbO_x through WO_{3-x}, rather than the slower direct discharging of NbO_x, is promoted by the mesoscale architecture.

To better understand the nature of the porous network, a composite film with the same architecture but covered with a thin, dense layer of pure NbO_x was fabricated. Ellipsometric porosimetry of a pure NbO_x film prepared from the POM revealed no apparent porosity, so we consider this layer to effectively block electrolyte access to the mesopores. Incorporating this overlayer completely changes the spectroelectro-chemical characteristics of the composite, which now no longer exhibits either selective VIS-NIR modulation or fast switching, although strong optical modulation can still be observed at long times (Supporting Information Figure S6). The slow kinetics are especially apparent for discharging, which takes an excessively long time (10 h) because the overlayer of NbO_x effectively generates a barrier for ion extraction from the WO_{3-x}. Optical measurements (Supporting Information Figure S6) reveal that a majority of the charge in WO_{3-x} and also a

Figure 3. Optical and electrochemical performance of architected nanocomposite films. (a) Transmittance spectra of the 260 nm-thick WO_{3-x}−NbO_x composite film on a ITO-coated glass at different switching potentials [vs Li/Li$^+$ in 0.1 M Li-TFSI/tetraglyme] and the corresponding photos of the sample. (b) Normalized charging profiles following potentiostatic steps for three different films: mesoporous WO_{3-x} nanocrystal framework (blue), NbO_x glass (orange), and the architected WO_{3-x}−NbO_x composite film (magenta). The discharging profile (at 4 V) of the composite film overlaps almost exactly with that of the empty WO_{3-x} framework. (c) Schematic energy diagram showing the charge flows in the architected composite at different switching potentials. Orange arrows indicate charging at 2.3 and 1.5 V. The dotted gray arrow indicates slow, direct discharging of NbO_x and the thick gray arrows indicate fast discharging of WO_{3-x} and NbO_x through WO_{3-x} according to the observed kinetics shown in (b). (d) Normalized charge capacity profiles of the same three films over 2000 cycles. Each sample was cycled by cyclic voltammetry between 1.5−4 V with a sweep rate selected to obtain a charge capacity above 70% of the saturated values under chronoamperometry at 1.5 and 4 V: (NbO_x at 10 mV/s, WO_{3-x} at 30 mV/s, and WO_{3-x}−NbO_x at 20 mV/s).

than either of the component materials (Table 2). In the NIR, the composite achieves 2.8-fold higher contrast than a

large portion of the charge in NbO_x are kinetically trapped due to this unfavorable energy alignment. Hence, the open network of mesopores is essential for the performance of our architected nanocomposite.

Other methods for in-filling of a mesoporous framework, such as atomic layer deposition,[36] typically result in conformal coatings and core−shell structures because the affinity of the two components is a prerequisite for deposition. The trade-off between electrochemical activity and the pore-filling ratio is thought to be inevitable. Our result suggests this hurdle can be overcome by introducing interface-sharing pore channels, which are produced in this work by a straightforward glass condensation process. As an added advantage, the electrochemical instability of the $WO_{3−x}$ nanocrystal film is also mitigated, as evaluated by a cycling durability test. Only 5.7% of the charge capacity of the architected composite was lost after 2000 cycles, whereas single component $WO_{3−x}$ and NbO_x films lost 21% and 11%, respectively (Figure 3d). This difference may result from the composite architecture being mechanically robust compared to the potentially degradable morphology of the unsupported nanocrystal framework.

In summary, every aspect of the nanocomposite architecture contributes to its electrochemical efficiency. Having been effectively templated by the $WO_{3−x}$ framework, the pore channels form an open network permitting the infiltration of the electrolyte to be in contact with both $WO_{3−x}$ and NbO_x, so that each component can be switched independently via electrochemical charging and discharging. Ion intercalation depth is also reduced to the size of the $WO_{3−x}$ nanocrystals and the size of the NbO_x mesodomains, as determined by the periodicity of the framework; this scaling can minimize the switching time. Furthermore, the coexistence of the pore channels with the covalently linked $WO_{3−x}$−NbO_x heterointerface establishes a redox cascade based on the relative alignment of the redox potentials, which favorably enhances the charging and discharging kinetics. The optical dynamic ranges of both active components are enhanced by the designer architecture. The results demonstrated here not only represent a practical dual-band electrochromic performance for energy-saving smart windows but also exemplify a broadly applicable approach toward constructing highly functional electrochemical materials (e.g., batteries, supercapacitors, and solar cells) by a synergistic arrangement of multiple components and their interfaces at the mesoscopic scale.

■ ASSOCIATED CONTENT

ⓢ Supporting Information

Methods, solar radiation spectrum, nanocrystal size distribution, cyclic voltammetry, detailed electrochromic switching, and ellipsometric porosimetry data. The Supporting Information is available free of charge on the ACS Publications website at DOI: 10.1021/acs.nanolett.5b02197.

■ AUTHOR INFORMATION

Corresponding Author

*E-mail: milliron@che.utexas.edu.

Notes

The authors declare the following competing financial interest(s): DJM has a financial interest in Heliotrope Technologies, a company pursuing commercial development of electrochromic devices.

■ REFERENCES

(1) Munch, E.; Launey, M. E.; Alsem, D. H.; Saiz, E.; Tomsia, A. P.; Ritchie, R. O. *Science* **2008**, *322*, 1516−1520.

(2) Ji, X.; Lee, K. T.; Nazar, L. F. *Nat. Mater.* **2009**, *8*, 500−506.

(3) Zheng, G.; Yang, Y.; Cha, J. J.; Hong, S. S.; Cui, Y. *Nano Lett.* **2011**, *11*, 4462−4467.

(4) Liu, N.; Lu, Z.; Zhao, J.; McDowell, M. T.; Lee, H.-W.; Zhao, W.; Cui, Y. *Nat. Nanotechnol.* **2014**, *9*, 187−192.

(5) Zhang, H.; Yu, X.; Braun, P. V. *Nat. Nanotechnol.* **2011**, *6*, 277−281.

(6) Zukalová, M.; Zukal, A.; Kavan, L.; Nazeeruddin, M. K.; Liska, P.; Grätzel, M. *Nano Lett.* **2005**, *5*, 1789−1792.

(7) Scherer, M. R. J.; Steiner, U. *Nano Lett.* **2013**, *13*, 3005−3010.

(8) Choi, S. Y.; Mamak, M.; Coombs, N.; Chopra, N.; Ozin, G. A. *Nano Lett.* **2004**, *4*, 1231−1235.

(9) Yu, G.; Gao, J.; Hummelen, J. C.; Wudl, F.; Heeger, A. J. *Science* **1995**, *270*, 1789−1791.

(10) Halls, J. J. M.; Walsh, C. A.; Greenham, N. C.; Marseglia, E. A.; Friend, R. H.; Moratti, S. C.; Holmes, A. B. *Nature* **1995**, *376*, 498−500.

(11) Llordes, A.; Garcia, G.; Gazquez, J.; Milliron, D. J. *Nature* **2013**, *500*, 323−326.

(12) Li, G.; Shrotriya, V.; Huang, J.; Yao, Y.; Moriarty, T.; Emery, K.; Yang, Y. *Nat. Mater.* **2005**, *4*, 864−868.

(13) Garcia, G.; Buonsanti, R.; Runnerstrom, E. L.; Mendelsberg, R. J.; Llordes, A.; Anders, A.; Richardson, T. J.; Milliron, D. J. *Nano Lett.* **2011**, *11*, 4415−4420.

(14) Garcia, G.; Buonsanti, R.; Llordes, A.; Runnerstrom, E. L.; Bergerud, A.; Milliron, D. J. *Adv. Opt. Mater.* **2013**, *1*, 215−220.

(15) Manthiram, K.; Alivisatos, A. P. *J. Am. Chem. Soc.* **2012**, *134*, 3995−3998.

(16) Mattox, T. M.; Bergerud, A.; Agrawal, A.; Milliron, D. J. *Chem. Mater.* **2014**, *26*, 1779−1784.

(17) Choi, S.-I.; Nam, K. M.; Park, B. K.; Seo, W. S.; Park, J. T. *Chem. Mater.* **2008**, *20*, 2609−2611.

(18) Kanehara, M.; Koike, H.; Yoshinaga, T.; Teranishi, T. *J. Am. Chem. Soc.* **2009**, *131*, 17736−17737.

(19) Lounis, S. D.; Runnerstrom, E. L.; Bergerud, A.; Nordlund, D.; Milliron, D. J. *J. Am. Chem. Soc.* **2014**, *136*, 7110−7116.

(20) Buonsanti, R.; Llordes, A.; Aloni, S.; Helms, B. A.; Milliron, D. J. *Nano Lett.* **2011**, *11*, 4706−4710.

(21) Buonsanti, R.; Pick, T. E.; Krins, N.; Richardson, T. J.; Helms, B. A.; Milliron, D. J. *Nano Lett.* **2012**, *12*, 3872−3877.

(22) Baklanov, M. R.; Mogilnikov, K. P.; Polovinkin, V. G.; Dultsev, F. N. *J. Vac. Sci. Technol., B: Microelectron. Process. Phenom.* **2000**, *18*, 1385−1391.

(23) Agrawal, A.; Kriegel, I.; Milliron, D. J. *J. Phys. Chem. C* **2015**, *119*, 6227−6238.

(24) Williams, T. E.; Chang, C. M.; Rosen, E. L.; Garcia, G.; Runnerstrom, E. L.; Williams, B. L.; Koo, B.; Buonsanti, R.; Milliron, D. J.; Helms, B. A. *J. Mater. Chem. C* **2014**, *2*, 3328−3335.

(25) Wang, J.; Polleux, J.; Lim, J.; Dunn, B. *J. Phys. Chem. C* **2007**, *111*, 14925−14931.

(26) Granqvist, C. G. *Sol. Energy Mater. Sol. Cells* **2000**, *60*, 201−262.

(27) Niklasson, G. A.; Granqvist, C. G. *J. Mater. Chem.* **2007**, *17*, 127−156.

(28) Özer, N.; Rubin, M. D.; Lampert, C. M. *Sol. Energy Mater. Sol. Cells* **1996**, *40*, 285−296.

(29) Villa, E. M.; Ohlin, C. A.; Balogh, E.; Anderson, T. M.; Nyman, M. D.; Casey, W. H. *Angew. Chem.* **2008**, *120*, 4922−4924.

(30) Llordes, A.; Hammack, A. T.; Buonsanti, R.; Tangirala, R.; Aloni, S.; Helms, B. A.; Milliron, D. J. *J. Mater. Chem.* **2011**, *21*, 11631−11638.

(31) DeForest, N.; Shehabi, A.; Garcia, G.; Greenblatt, J.; Masanet, E.; Lee, E. S.; Selkowitz, S.; Milliron, D. J. *Build. Environ.* **2013**, *61*, 160−168.

(32) Beaujuge, P. M.; Ellinger, S.; Reynolds, J. R. *Nat. Mater.* **2008**, *7*, 795−799.

(33) Granqvist, C. G. *Thin Solid Films* **2014**, *564*, 1−38.

(34) Ozkan, E.; Lee, S.-H.; Liu, P.; Tracy, C. E.; Tepehan, F. Z.; Pitts, J. R.; Deb, S. K. *Solid State Ionics* **2002**, *149*, 139−146.

(35) Deepa, M.; Srivastava, A. K.; Sood, K. N.; Agnihotry, S. A. *Nanotechnology* **2006**, *17*, 2625.

(36) George, S. M. *Chem. Rev.* **2010**, *110*, 111−131.